Qualification of Active Cooling Concepts in Ground Facilities

B. Esser and A. Gülhan

Deutsches Zentrum für Luft- und Raumfahrt (DLR)
Abteilung Windkanäle
des Instituts für Aerodynamik und Strömungstechnik
Linder Höhe, D-51147 Köln, Germany
burkard.esser@dlr.de

Summary

Two active cooling concepts were tested concerning their capabilities with respect to surface cooling in hypersonic flow. Film cooling was analysed in cold hypersonic flow at realistic Reynolds numbers. Cooling efficiency was found highly sensitive to injection geometry and flow inclination. Best performance was observed for helium with a heat flux reduction up to 90% compared to the non-cooled case. Transpiration cooling was thermally qualified in high enthalpy flow. The coolant was supplied through a porous material integrated in the surface. Substantial cooling could be achieved in the injection area and further downstream at low coolant flow rates. Optimal flow rates could be identified for several coolants.

1 Introduction

Reliable qualification of key technologies for future space vehicles, as e.g. improved cooling concepts basing on new material developments, is not possible without dedicated experiments in ground test facilities. Although the capabilities of numerical simulations have significantly improved in the past decades, the thermo-mechanical behaviour of highly loaded components of space vehicles during the hot phase of atmospheric entry can be predicted with larger restraints only, even for state-of-the-art technologies. New developments need additional experimental investigation in test facilities that are able to establish high enthalpy hypersonic flow conditions for time periods that are characteristic for atmospheric entry, i.e. at least several minutes. These requirements are met by the LBK facility which is one of the European key facilities for qualification of thermal protection systems. In LBK realistic combinations of convective and radiative heat loads can be applied and components can be tested in an atmosphere with a realistic gas composition at realistic Mach numbers. Other parameters, as e.g. Reynolds numbers, binary scaling factors and boundary layer thickness, cannot be duplicated in such facilities, in general. Therefore, a combined investigation with other ground test facilities is required to match all important parameters. Possible complementary facilities are short-duration high enthalpy facilities, as e.g. shock tunnels, that provide realistic Reynolds and Mach numbers, or cold hypersonic facilities, as e.g. the hypersonic windtunnel H2K,

A. Gülhan (Ed.): RESPACE – Key Tech. for Reusable Space Sys., NNFM 98, pp. 104–131, 2008.
springerlink.com

where boundary layer transition can be simulated at realistic Reynolds numbers, but on a low surface temperature level.

Two separate investigations were performed that represent two stages of the above mentioned combined ground testing philosophy. The first activity was strongly linked to cooling concept that is described in section 6. It focused on the thermal qualification of transpiration cooling in the arc heated facility LBK. All parameters that transpiration cooling is presumed to depend on, i.e. porous material, coolant gas, and coolant mass flow rate, were systematically varied in order to identify their influence on cooling efficiency. The second activity was carried out in the cold hypersonic windtunnel H2K and was linked to the investigations on film cooling concepts that are presented in sections 8 and 9. Details of this activity are reported in section 2, the qualification of transpiration cooling will follow in section 3.

2 Film Cooling in Cold Hypersonic Flow

Film cooling has been found to be one of the most efficient measures to protect propulsion components from high aerothermal loads [6, 7, 8, 12, 15]. But its application for external aircraft components, in particular in hypersonic flows, has still to be developed and demonstrated. Therefore, in the frame of this work the feasibility of film cooling for the protection of external hot structures in the hypersonic flow regime was investigated. A wedge model with variable injection geometry and cooling medium was used to perform a systematic experimental study in DLR's hypersonic wind tunnel H2K. In addition to feasibility information the experiments were expected to provide a better understanding of film cooling physics for a hypersonic flight environment.

Infrared thermography was used to measure the temperature distribution on the model surface. By using a material with a low thermal conductivity for the principal parts of the model surface the heat flux distribution could be determined from the measured surface temperature history. In combination with Schlieren pictures these measurements were used to interpret the boundary layer flow properties, the influence of free stream flow parameters, different coolant injection geometries, and flow parameters of the coolant.

The tests were performed at a Mach number of 6 and two different Reynolds numbers. The variation of the Reynolds number should allow to identify the conditions for a possible undesired boundary layer transition.

2.1 Wedge Model

A wedge model consisting of a nose with 45° wedge angle and a downstream flat plate as shown in Fig. 1 was used for the wind tunnel experiments. In order to study different parameters the model was designed in a modular way. It consists of three main components: a wedge type nose, a coolant injection slot and the main body with a flat plate on the flow side. The main body was mounted to the H2K model support system by screws.

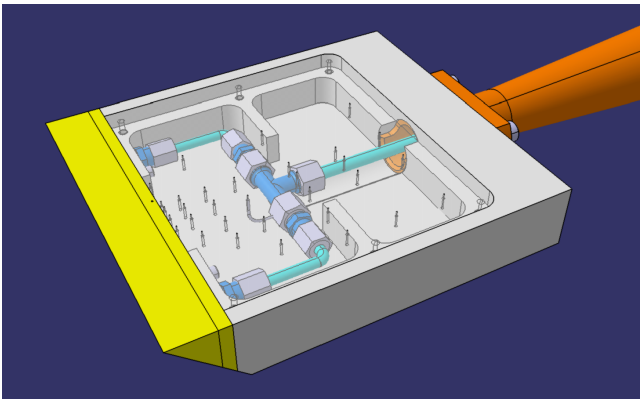

Fig. 1. 3D-view of the H2K wedge model

The nose part and the injection slot could be changed. Two different noses were available, one with a sharp edge and a blunt nose with a radius of 5 mm. The wedge angle was 45° for both. Variation of the nose part allowed to check the influence of the boundary layer thickness and entropy layer on the results. Different injection slots could be placed between the nose and the flat plate part. They were connected to a coolant reservoir inside the model's main body. The reservoir was equipped with a pressure and a temperature sensor.

The flat plate on top of the main body was made of PEEK material. Due to its emissivity value of 0.95 and its low thermal conductivity PEEK is well suited for heat flux determination from infrared spectroscopy. It is applicable at temperatures between –65°C and 250°C. Its thermal properties at room temperature are listed in Table 1. The properties change with temperature and a linear correlation was applied for the determination of heat flux rates from measured surface temperatures.

Table 1. Material properties of PEEK at 20°C

property	
Surface emissivity [–]	0.95
Thermal conductivity [W/(mK)]	0.25
Density [kg/m^3]	1320
Specific heat [J/(kgK)]	1656

2.2 Test Parameters

The main test parameters were the free stream conditions, model geometry, coolant gas and coolant injection. At a common Mach number of 6 two free stream conditions with a significantly different Reynolds number were applied. The main parameters are listed in Table 2. Furthermore, tests were performed at two angles of attack, i.e. $\alpha = 0°$ and $\alpha = 20°$. The corresponding model coordinate system is shown in Fig. 2.

Table 2. Free stream parameters

Parameter	FC-A	FC-B
Reynolds number [1/m]	$2.8 \cdot 10^6$	$14.3 \cdot 10^6$
Total temperature [K]	730	470
Reservoir pressure [bar]	6.0	16.5
Flow rate (free stream) [kg/(m^2 s)]	16.85	57.75
Flow rate (post-shock, $\alpha = -20°$) [kg/(m^2 s)]	55.56	190.4

Air, argon and helium were used as coolants. They were chosen in order to achieve sufficient difference in heat capacity, thermal conductivity, and density. The main properties of the coolant gases are listed in Table 3.

Table 3. Thermodynamic properties of coolants

Thermodynamic property	Air	Helium	Argon
Molar mass [kg/kmol]	28.96	4.003	39.95
Density (at standard conditions) [kg/m^3]	1.2929	0.1785	1.784
Specific heat at constant pressure [J/(kgK)]	1007	5238	524
Specific heat at constant volume [J/(kgK)]	720	3214	323
Ratio of specific heats [–]	1.40	1.63	1.62
Gas constant [J/(kgK)]	287	2024	201
Thermal conductivity [10^{-3} W/(mK)]	25.6	148	17,3
Dynamic viscosity [10^{-6} kg/(ms)]	18.19	19.6	22.11
Prandtl number [–]	0.72	0.69	0.66

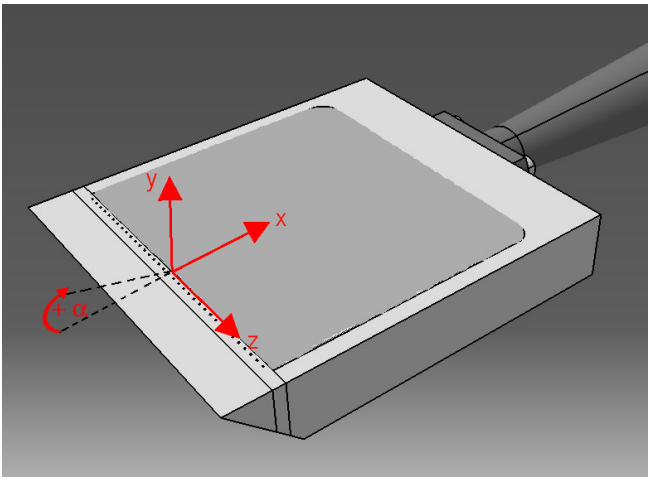

Fig. 2. Model with definition of coordinate system

The coolant mass flow rate could be varied between 0 and 0.8 g/s. For the comparison of cooling efficiency the blowing ratio

$$F = \frac{(\rho u)_{coolant}}{(\rho u)_e} \tag{1}$$

was used which relates the coolant flow rate

$$(\rho u)_{coolant} = \dot{m}_{coolant} \Big/ A_{injection} \tag{2}$$

to the external flow rates at the boundary layer edge which are included in Table 2 for the two angles of attack.

The geometry of coolant injection was an important test parameter. Due to the modular model design it could be changed easily by changing the injection slot. Six injection slots were used during the test campaign. The corresponding hole configurations are listed in Table 4 The diameter of holes was either 0.5 mm or 1 mm.

Single hole injection was used for orthogonal injection only. Slots with multiple holes aligned in a row with a distance of 5 mm between the holes were used for orthogonal injection, for oblique injection at an angle of 30° to the surface and for tangential injection. For slots R3 and R4 the holes were placed on one half of the slot area.

Table 4. Injection slots

Name	Type	Number of holes	Diameter of holes [mm]	Injection angle
S1	Single hole	1	1.0	90°
S3	Single holes	3	1 x 0.5 and 2 x 1.0	90°
R1	Row of holes	35	1.0	90°
R2	Row of holes	34	0.5	90°
R3	Row of holes	17	0.5	30°
R4	Row of holes	17	0.5	0°

2.3 Experimental Results with Orthogonal Injection

First tests were carried out on a configuration S3 with three single holes, one 0.5 mm wide and two 1 mm. Air and argon were used as coolant. As the infrared images in Fig. 3 show, the thermal effects are very similar for air and argon at a coolant flow rate of 0.01 g/s. Distinct horizontal streaks are visible that emanate from the injection hole. The streaks correspond to vortices in the main flow which are generated by local flow separation at the locations of coolant injection, even at flow condition A with the low Reynolds number. Separation and re-attachment shocks as well as re-attaching vortices lead to a strong local aerothermal heating [2, 9].

The effect is more intense for 1 mm holes, but for the 0.5 mm hole, which is located in the lower part of the IR image, it is still obvious. Therefore, injection configuration S3 causes local heating instead of cooling.

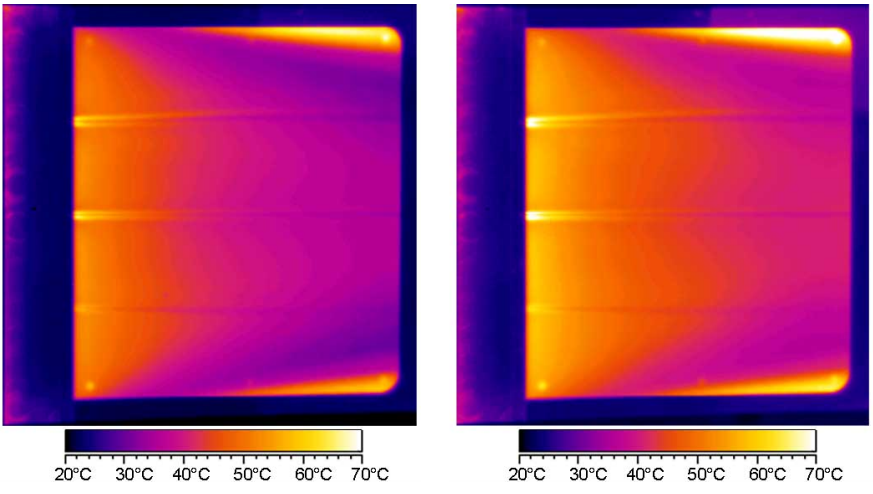

(a) air (b) argon

Fig. 3. Air and argon injection at 0.01 g/s (F = 0.34) through single holes with 0.5 mm and 1 mm diameter

Injection slot R2 (34 holes of 0.5 mm) causes similar heating phenomena at a total coolant mass flow rate of 0.02 g/s, although the flow rate per hole is significantly lower. The corresponding infrared images are shown in Fig. 4. Compared to air and argon the aerothermal heating appears more intense for helium cooling indicating a more significant disturbance of the main flow for this gas. Helium has a significantly lower density compared to the other two gases. Therefore, its volume is much higher causing a stronger disturbance to the laminar boundary layer.

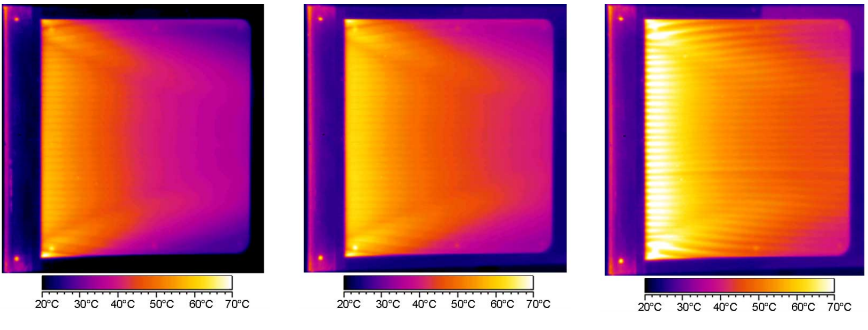

(a) air (b) argon (c) helium

Fig. 4. Air, argon and helium injection at 0.02 g/s (F = 0.18) through a row of 34 holes with 0.5 mm

Aerothermal heating increases with larger coolant mass flow rates. For single hole injection with slot S1 the heating caused by re-attachment of separated flow and vortices becomes stronger for the high coolant flow rates ($F = 5.74$) as shown in

Fig. 5. Similar results were obtained for slot R2. The infrared images in Fig. 6 indicate a stronger aerothermal heating when the coolant mass flow rate is increased by a factor of two.

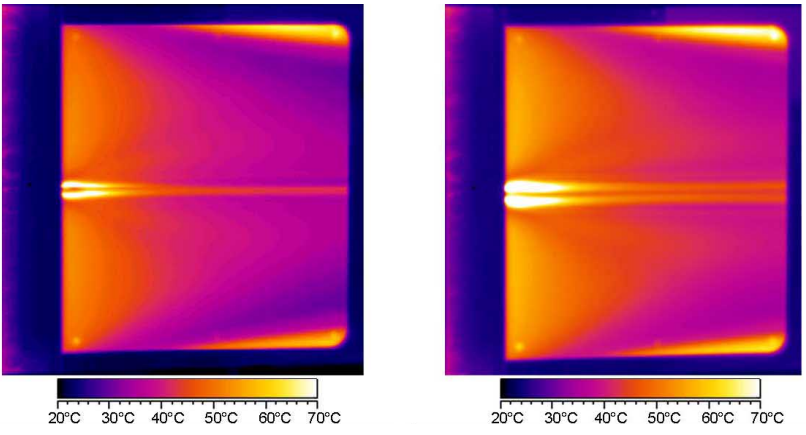

(a) $F = 2.04$ (b) $F = 5.74$

Fig. 5. Cold air injection with slot S1 at flow rates of 0.027 g/s (F = 2.04) and 0.076 g/s (F = 5.74)

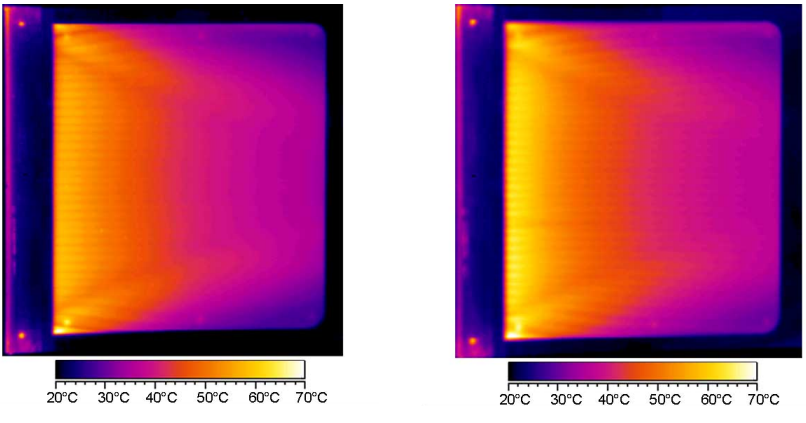

(a) $F = 0.18$ (b) $F = 0.36$

Fig. 6. Cold air injection with slot R2 at different flow rates of 0.02 g/s (F = 0.18) and 0.041 g/s (F = 0.36)

2.4 Experimental Results with Tangential Injection

All tests with orthogonal injection showed that the boundary layer is disturbed by the coolant causing aerothermal heating instead of cooling. Since the situation could not significantly be improved by reducing the injection angle from 90° to 30°, it was

decided to change injection to tangential injection with slot R4. It was realized by mounting a deflection plate above the injection part for orthogonal injection.

In order to see the effect of cooling instantaneously only one half of the injection slots was used for the cold gas injection. The infrared images in Fig. 7 show that the lower part is not cooled and could be used as reference. The figures correspond to different coolant mass flow rates. At the lowest mass flow rate of 0.039 g/s ($F = 0.69$) cooling is observed in a very narrow area close to the injection slot. Further downstream there is no significant difference between the cooled part and the reference surface.

Increasing the coolant mass flow rate to 0.187 g/s the cooled surface area downstream the injection increases. Except for the lateral boundaries of the cooled area no heating caused by the vortices or boundary layer tripping has been noticed. At the highest mass flow rate of 0.383 g/s cooling is strong as well close to the injection. But further downstream the pattern becomes more streaky indicating a increasing heat transfer to the surface increases due to vortex attachment and boundary layer tripping. At one location of the reference model the surface is heated due to similar effects downstream of a leak in the injection slot.

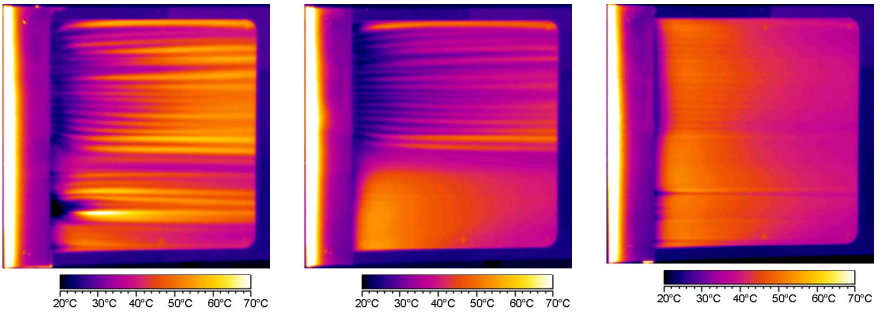

(a) $F = 6.81$ (b) $F = 3.32$ (c) $F = 0.69$

Fig. 7. IR images of tests at $\alpha = 0°$ with air cooling at injection rates of 0.383 g/s (F = 6.81), 0.187 g/s (F = 3.32), 0.039 g/s (F = 0.69)

A comparative technique is applied for the analysis of the test results. On the cooled side, Stanton numbers are evaluated along a line oriented in flow direction. Afterwards, the Stanton number distribution is determined for the corresponding line on the reference side. So, the ratio between the Stanton numbers indicates the cooling efficiency. By this procedure influences from geometry and free stream properties are eliminated. Cooling is effective as long as the ratio between cooled and non-cooled Stanton number remains below unity. A ratio above 1 corresponds to ineffective cooling, since in this case the heat on the cooled side is larger than the non-cooled reference.

In Fig. 8 Stanton number ratios are compared for three tests with air as coolant at different mass flow rates. At the lowest mass flow rate of 0.039 g/s cooling is restricted to the immediate vicinity of the injection area as it had already been

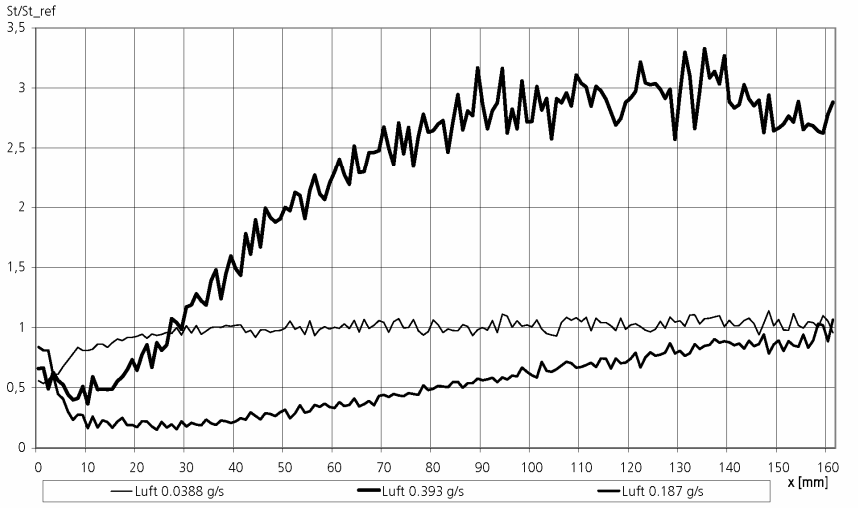

Fig. 8. Stanton number ratios in axial direction for different injection rates of air

observed from Fig. 7. From a location 20 mm downstream the ratio is close to 1, indicating no difference between cooled and reference side.

At a coolant flow rate of 0.187 g/s effective cooling is achieved along the complete length of the PEEK plate. Best cooling is provided at distances between 10 mm and 30 mm from the injection. Here the heat flux to the surface is reduced to 20% of the reference. Further downstream, the Stanton number ratio gradually increases. The efficiency of cooling decreases due to a disintegration of the coolant film.

Doubling the injection rate to a value of 0.383 g/s gives rise to a completely different behaviour. Due to increased shear stress the coolant film becomes unstable tripping the boundary layer. Cooling is observed within the first 30 mm only. Further downstream the heat load to the surface is increased significantly, partially reaching up to 300% of the non-cooled value.

At an injection rate of about 0.19 g/s, where the most effective cooling was observed in air, tests were performed with argon and helium as well. In Fig. 9 the Stanton number ratios of all three coolants are compared. The general behaviour is similar. Effective cooling is observed along the complete length. Maximal efficiency is achieved close to the injection, further downstream the efficiency gradually decreases.

Along the first 20 mm there is no remarkable difference between the coolants. In that region, cooling is dominated by model geometry. The backward facing step at the coolant injection generates a detached flow with a recirculation near the surface that reduces heat flux. Differences between the particular coolants become evident further downstream. Compared to air, argon behaves almost identical along the first 40 mm with an identical minimum Stanton number ratio of 0.2. At larger distances to the coolant injection argon cooling is more efficient. At the end of the PEEK plate, where the potential of air cooling has exhausted, argon still provides a Stanton number ratio of 0.7.

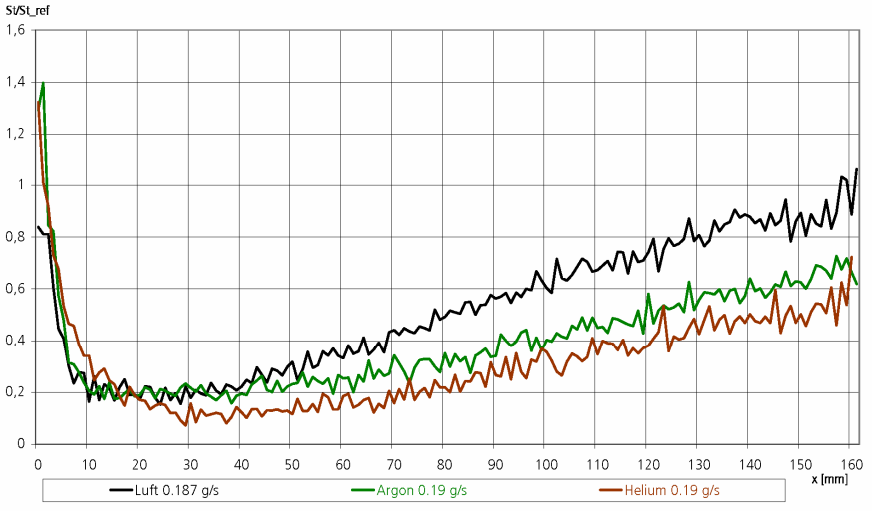

Fig. 9. Comparison of Stanton number ratios along an axial line for air, argon and helium cooling

Best performance, however, is obtained for helium cooling. It provides a reduction of the Stanton number to about 10% of the non-cooled reference and the efficiency remains best up to the end of the PEEK plate.

Differences between the coolants become evident in the infrared images as well (see Fig. 10). Compared to air cooling the surface temperature at the coolant injection is significantly lower with argon. In addition, the vortices at the sides of the cooled regime are more evident in the surface temperature distribution.

For helium the temperature difference between coolant injection and the end of the PEEK plate is lowest. In addition, the streak pattern on the cooled side is not as

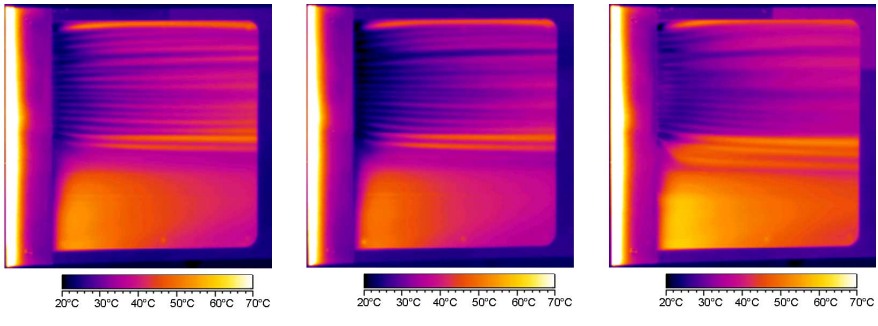

(a) air (b) argon (c) helium

Fig. 10. IR images of tests with different coolants at 0.19 g/s (F = 3.37)

pronounced as it is observed for air and argon, where individual coolant jets can be distinguished much better. There is a penetration of coolant into the reference side for all three coolants, but helium seems to penetrate farther than air and argon.

The better performance of helium can be explained by its heat capacity, which is about five times higher compared to air and 10 times higher compared to argon. But since argon performes better than air, heat capacity is not the only parameter that takes influence on cooling efficiency.

When the model is inclined to the flow by 20°, the effect of air cooling remains almost negligible at the lowest mass flow rate of 0.039 g/s. Just the recirculation area downstream of the coolant injection is more prominent than at $\alpha = 0°$ as comes out from the infrared image in Fig. 11. Streaks of individual coolant jets can be guessed

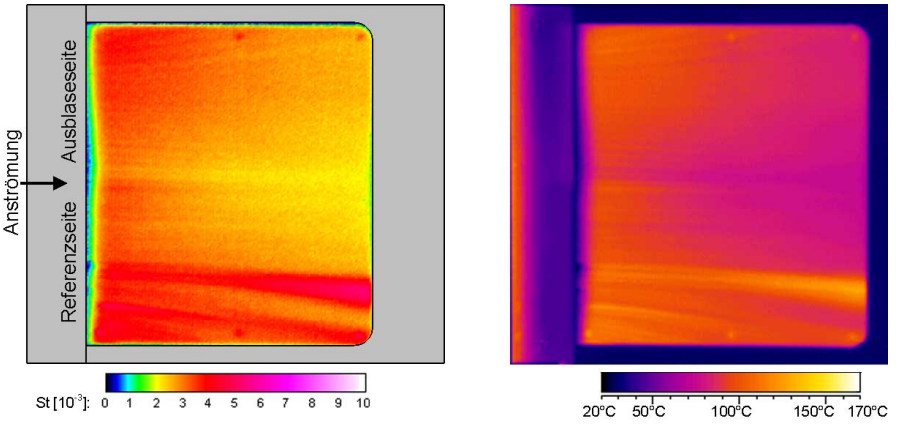

(a) Stanton number (b) Temperature

Fig. 11. Stanton number and surface temperature distribution for air cooling at 0.039 g/s (F = 0.21) and $\alpha = -20°$

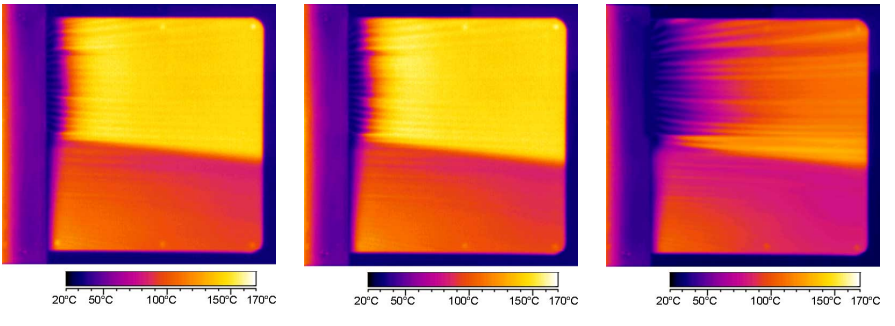

(a) air (b) argon (c) helium

Fig. 12. IR images of the tests at $\alpha = -20°$ with 0.184 g/s air, argon and helium cooling (F = 0.99)

only on the cooled side of the model. The clear streak on the non-cooled reference side refers to an unintended leakage.

Situation changes significantly when the injection rate is increased to 0.184 g/s. As comes out from the infrared images shown in Fig. 12 the recirculation area is enlarged compared to Fig. 11 due to the higher amount of injected gas. But at the downstream end of the recirculation area the boundary layer is tripped and the surface temperature is increased by about 50% compared to the non-cooled reference side.

Only minor differences are observed between air and argon. Downstream of the cool injection area there is a zone with a streaky flow pattern corresponding to boundary layer transition. Further downstream the temperature distribution is nearly homogeneous at an increased level.

The characteristics from the infrared images are confirmed by the Stanton number ratios shown in Fig. 13 which were evaluated along an axial line. The results for air and argon are almost identical, and cooling is obtained for the first 20 mm only. The minimum value is close to 0.2 which is comparable to the value at $\alpha = 0°$. In the transition regime which extends up to $x = 50$ mm the Stanton number ratio increases to a value of 2. Except for a minor increase along the last 30 mm, this level is kept until the end of the PEEK plate.

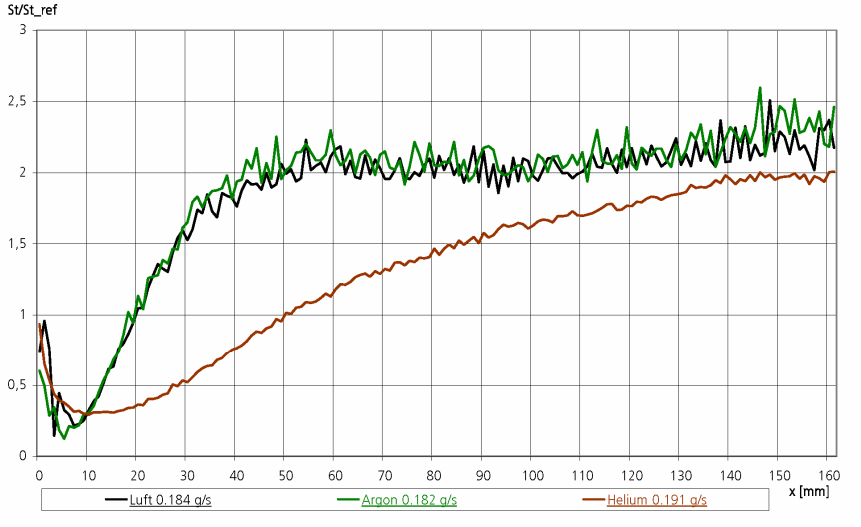

Fig. 13. Comparison of Stanton number ratios along an axial line for air, argon and helium cooling at α = -20° (F = 0.99)

At first glance, the situation is different for helium cooling. The infrared image shows a significantly larger cooling zone close to the injection. The Stanton number ratio remains below 1 for a section of 50 mm compared to 20 mm for air and argon. The temperature gradient inside the transition regime is smaller and the transition regime extends almost to the end of the plate. Along the plate's last 20 mm the Stanton number ratio is nearly constant at a value of 2. So, for all three gases the same

Stanton number ratio is achieved at the end of the transition zone. This gives rise to the assumption that the Stanton numbers ratios follow a common trend, but with a different characteristic length scale for helium compared to air and argon. The different length scale might be related to the sound velocity, which is almost identical for air and argon and more than three times larger for helium. Due to sonic injection the initial coolant velocity is significantly higher for helium which enables a deeper penetration into the boundary layer.

2.5 Concluding Remarks

An experimental investigation was performed on a flat plate model with respect to film cooling in the laminar hypersonic flow field of H2K at a free stream Mach number of 6. Model geometry, injection angle, coolant gas and free stream conditions were varied to find out their potential concerning the reduction of aerothermodynamical heat loads. An infrared camera system was applied to measure surface temperature distributions on the model and the corresponding heat loads were evaluated from the temperature evolution.

No cooling effect could be achieved when the coolant was injected perpendicular to the flow. Air, argon, and helium were applied as coolants, but no heat reduction was observed, neither for a single injection nor for multiple injections laterally aligned in a row. Instead of cooling locally enhanced heat loads were observed which increased with increasing coolant mass flow rate. Due to the orthogonal injection the coolant jets acted as obstacles in the hypersonic flow. At the injection area strong horseshoe-like vortices develop that are known to cause increased heat loads.

The situation could not be improved by reducing the injection angle from 90° to 30°. At substantial coolant mass flow rates the same behaviour was observed, weak cooling could be achieved for very low mass flow rates only.

Efficient cooling was obtained with tangential injection at the bottom of a backward facing step. At zero angle of attack all three coolants provided a substantial reduction of heat fluxes for a blowing ratio of 3.3 Best performance was observed for helium, which reduced the heat flux up to 90% compared to the non-cooled case. The maximum local heat flux reduction was 80% for air and argon. Since the cooled area extended further downstream, the global performance was slightly better for argon.

When the model was inclined to the flow by 20° the boundary layer got tripped for all coolants at substantial coolant mass flow rates with a blowing ration close to 1. The heat flux to the surface was enhanced compared to the non-cooled reference case. Heat enhancement was strong for air and argon and more moderate for helium.

3 High Enthalpy Qualification of Transpiration Cooled TPS

Thermal qualification of structures that are exposed to extreme thermal loads, e.g. during Earth re-entry or planetary entry, needs long-duration ground test facilities. During atmospheric entry thermal loading is a combination of convective and radiative heat loads. Due to the non-linear behaviour of radiation the scenario does not allow for thermal scaling, but needs testing at real temperature levels.

Transpiration cooling is assumed to be mainly influenced by the porous surface material, the coolant used, and the coolant's mass flow rate. These parameters were varied during the qualification test campaign in order to find their influence on cooling efficiency.

3.1 Test Facility

The tests on transpiration cooling were performed in DLR's arc heated facility LBK, which consists of the two tests legs L2K and L3K. The facility is one of the European key facilities for the qualification of thermal protection systems and can provide sufficient testing times and realistic atmospheric conditions for planetary entry. A sketch of the facility is plotted in Fig. 14, details can be found in [4, 3].

Central part of each test leg is an arc heater. At L2K, there is a Huels-type heater with an electrical power of 1 MW and at L3K a 6 MW segmented arc heater. Downstream of the arc heater the flow is accelerated to hypersonic velocities by conical nozzles with a half angle of 12°. Depending on the nozzle's exit diameter Mach numbers in the range from 4 to 10 can be achieved at stagnation pressures up to 350 hPa.

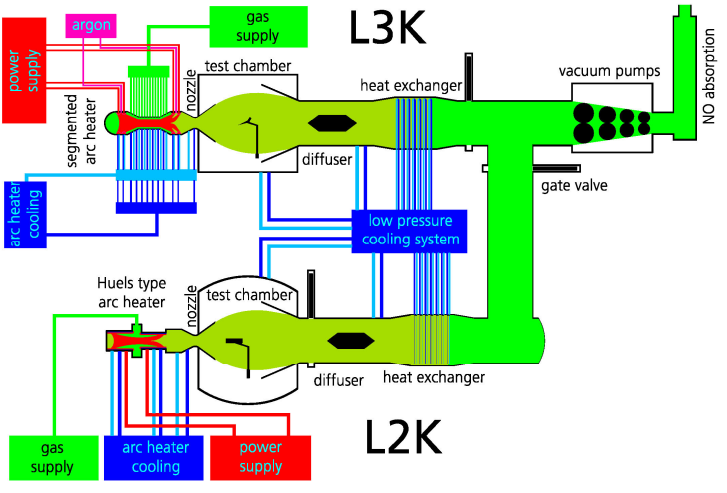

Fig. 14. Sketch of the LBK facility

During the project both tests legs have been used. First screening tests were run in L2K in order to check the applicability of transpiration cooling and the operation of the cooling supply systems. Afterwards testing was switched to the L3K facility, where higher enthalpy levels, surface temperatures and surface pressures can be achieved.

3.2 Model and Instrumentation

Thermal testing of transpiration cooled structures in a hypersonic high enthalpy flow field requires an experimental setup that allows for continuous coolant supply at

adjustable mass flow rates through a porous sample in the surface of windtunnel model. For reliable operation the porous sample was directly connected to a coolant reservoir inside the model. The coolant itself was supplied from K-bottles outside the test chamber with a controller installed in the supply line. This concept was checked in two screening test campaigns in L2K and L3K which are described in more detail in section 6. The general concept was approved by the screening tests, only details of the reservoir design had to be modified, e.g. adhesives were identified unsuitable for the connection between porous sample and reservoir.

For the final test campaign in the L3K facility a flat plate model was used as shown in Fig. 15. The porous sample was integrated on the model's left hand side (viewed in flow direction). Square 60 mm wide porous samples with a thickness of 6 mm were used. The samples were embedded in a plate of carbon reinforced silicon carbide (C/C-SiC) which is a well qualified reusable high-temperature thermal protection material. Detailed information on the C/C-SiC material is given in [5, 10]. Except for the porous sample the model is symmetric with respect to its mid plane in flow direction. The two sides differ by the porous sample only. Since the flow field is symmetric to the same plane as well, the non-cooled side could be used as reference.

The complete setup was installed on top of a water-cooled model holder with a blunt nose, which is water-cooled as well. The cubic coolant reservoir made of C/C-SiC was mounted just on top of the model holder's base plate. There are three connections to the reservoir's side wall (see Fig. 15a). The left one corresponds to the coolant supply line, the other two are connectors for measuring pressure and temperature inside the reservoir. Nitrogen, helium and argon were used as coolants, the coolant's mass flow rate could be set to 0.2-10 g/s.

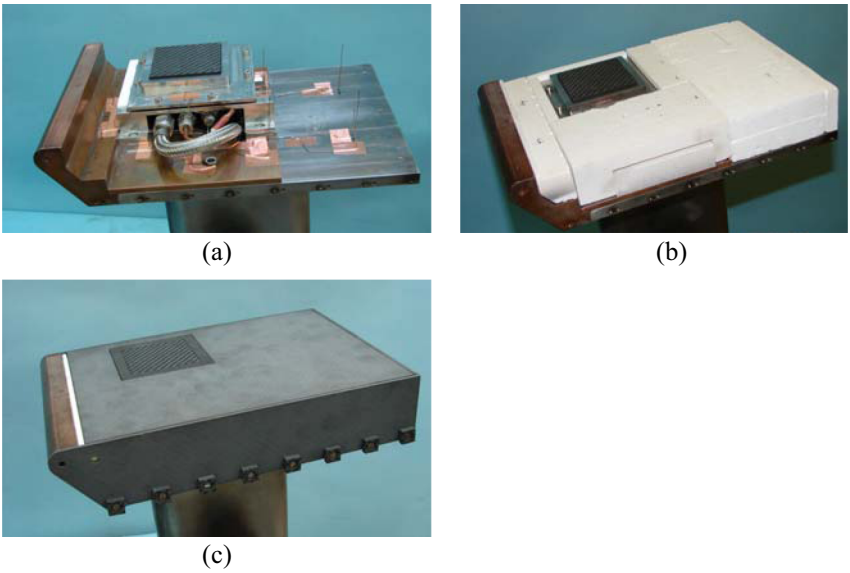

Fig. 15. Model for transpiration cooling testing

The porous sample ws installed on top of the reservoir. A tight connection was obtained by a carbon seal which was compressed by a jacket frame made of high-temperature alloy PM2000. The remaining space between the C/C-SiC plate on top and the base plate was filled with insulating material. The insulation prevented the aerothermal heating on the top from being influenced by the cooled parts of the model holder. Furthermore, the insulation material avoided internal radiation, which might lead to a substantial heating to the model's interior due to the expected high surface temperatures.

Three different porous sample materials were tested. Although all of them made of carbon reinforced carbon (C/C), there were differences with respect to porosity, permeability, and structural details. The majority of tests was peformed with samples made of "standard C/C" having a porosity of about 17%. This material is referenced as standard, since it had been successfully applied to transpiration cooling in a different environment, i.e. a combustion chamber [11, 14]. The "highly porous C/C" is similar to standard C/C, but with a porosity of 44%. Standard C/C and highly porous C/C have the carbon fibres oriented parallel to the top surface, while for the third type, "stratified C/C", the layers are oriented perpendicular to the surface. The main properties of all samples that were tested are listed in Table 5.

Table 5. Tested samples

Sample	Material	Porosity [%]
S1	Standard C/C	17
S2	Standard C/C	17
S3	Row of holes	17
H1	High porosity C/C	44
P1	Stratified C/C	16

The model was primarily instrumented for temperature measurements. In total 17 thermocouples were installed in the interior, 12 either directly below the C/C-SiC cover plate or inside the insulation material. The coolant's state in the reservoir was monitored during tests by a thermocouple and a pressure gauge. The remaining thermocouples were used to monitor the temperatures of reservoir walls, sample and base plate. The locations of the thermocouples are plotted in Fig. 16.

In addition to the temperature measurements inside the model the surface temperature distribution was measured by infrared cameras. During all tests a camera with a high temperature measuring range between 350°C and 2000°C was used. The temperature range was well-suited for the non-cooled parts of the surface. For the porous probe, however, the camera was working near to or even below its low temperature limit. In order to obtain a better temperature of this particular area a second infrared camera was added which was set for measurements in the range of 0–500°C. The camera measurements were supported by pyrometer measurements at specific spots on the surface, i.e. the centre of the porous sample, the corresponding location on the non-cooled side, and a location upstream of the sample. Since the pyrometers work in the near infrared range close to 1 µm, their measurements are almost not affected by uncertainties in the surface material's emissivity. Therefore

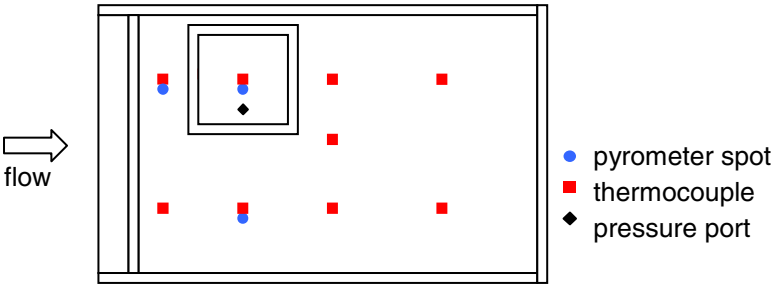

Fig. 16. Pyrometer spots and locations of intrusive measurements

they could be used to correct the results of the infrared cameras which operate in the far infrared regime with regard to surface emissivity [1].

3.3 Flow Condition and Test Parameters

A nozzle with a throat diameter of 29 mm and an exit diameter of 300 mm was used for the tests. Air was used as working gas. Based on the facility's operating conditions the nozzle flow field was computed using the CEVCATS-N code [13]. The computation includes the effects of non-equilibrium thermodynamics and chemistry. The resulting Mach number distribution along the nozzle is plotted in Fig. 17. The flow Mach number increases almost uniformly along the nozzle. In lateral direction the flow field is nearly homogeneous providing constant flow properties along the width of the model which is placed 300 mm downstream of the nozzle exit area. The flow properties that were obtained at model location are listed in Table 6 together with the operating conditions.

All tests were performed according to an identical test procedure. After ignition of the arc heater the flow conditions were gradually changed during facility startup until the desired operating conditions had been achieved. During this period the model was

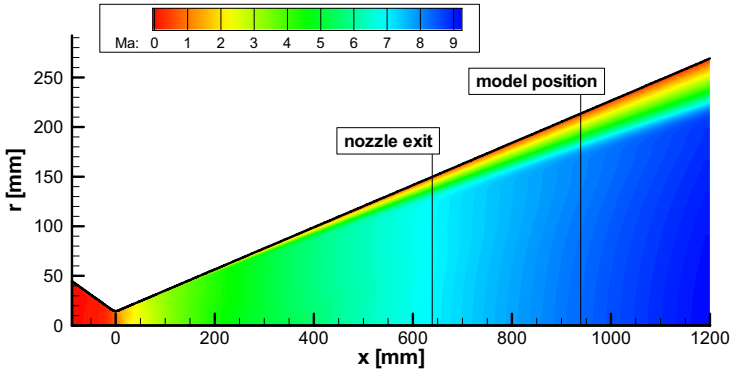

Fig. 17. L3K flow field

placed outside the flowfield in the background area of the test chamber in order to avoid the measurements from being influenced by changing flow conditions. During this period the transpiration cooling system was started as well.

As soon as the desired flow conditions were reached and the coolant was being supplied at the defined mass flow rate, the test was started by moving the model to the axis of the flow field. Here, the model remained for the specified test duration which was either 180 s or 240 s. After this period, the model was moved out of the flow field, and the flow was stopped. Data acquisition was continued for about five more minutes, since the cooling phase provides additional information about the heating of the model.

Table 6. Facility operating conditions and flow conditions at model location

Reservoir pressure	[hPa]	4700
Reservoir temperature	[K]	5650
Total enthalpy	[MJ/kg]	11.6
Mach number	[–]	7.5
Free stream pressure	[Pa]	56
Free stream temperature	[K]	530
Free stream velocity	[m/s]	3873
N_2 mass fraction	[–]	0.762
O_2 mass fraction	[–]	0.004
NO mass fraction	[–]	0.007
N mass fraction	[–]	$< 10^{-4}$
O mass fraction	[–]	0.227

3.4 Test Results

Transpiration cooling of a structure in a high-enthalpy, hypersonic flow is mainly influenced by the applied porous material, the coolant used, and the coolant's mass flow rate. The objective of the test campaign in L3K was to investigate the influence of these parameters on the thermal behaviour of the model for two different heat loads which were generated by varying the model's angle of attack between 20° and 30°. Due to the high number of test parameters "standard C/C" was defined as baseline material and nitrogen as baseline coolant. Accordingly, tests with different coolants were performed on "standard-C/C" samples and systematic variations of the coolant mass flow rate were carried out with nitrogen cooling.

Individual tests were performed at constant coolant mass flow rate. Therefore, in one test only a single combination of parameters could be tested. Proceeding that way, the facility must be able to reproduce identical test conditions during subsequent runs. Figure 18 shows the results of pyrometer and thermocouple measurements from three tests at an angle of attack of 20°. The measurements were taken on the non-cooled reference side at a location that corresponds to the centre of the porous sample. The testing time was 180 s for all three tests. This period is marked by a red background colour. The signals coincide well proving the required reproducibility.

At the end of the testing time the surface temperature which is measured by the pyrometer reached a steady state level of 1015°C. Since the pyrometer has a low

temperature limit of 900°C, the measurement becomes physical when the surface temperature is exceeding this limit. During the first 55 seconds the pyrometer signal is set by the internal electronics to an artificial value. The thermocouple which is placed 3 mm below the surface starts rising almost immediately when the model is moved into the flow field. At the end of the test it indicates a nearly constant temperature of 955°C.

When the heat load is increased by changing the angle of attack to 30° the surface temperature reaches 1170°C after 180 seconds testing as shown in Fig. 19. Below the cover plate, the temperature increases to 1120°C as indicated by the thermocouple measurements. Again, the temperature difference across the cover plate is close to 50 K, which agrees to the thermal properties of the material. The agreement of both, pyrometer and thermocouples signals, show a good agreement proving the reproducibility of test conditions at the higher heat load as well.

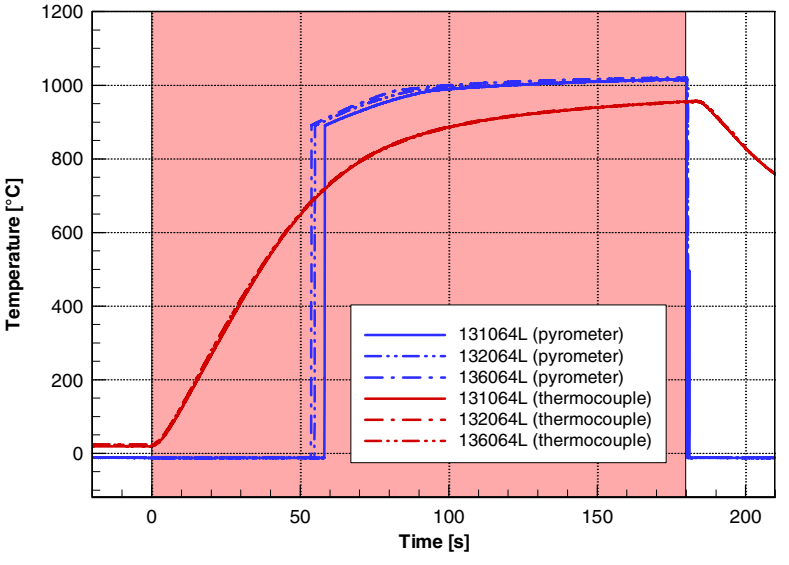

Fig. 18. Pyrometer and thermocouple measurements at the reference location from three tests at $\alpha = 20°$

The non-cooled side of the model also provides a kind of technological reference with regard to results of transpiration cooling, since the surface is completely made of reusable TPS material that is able to withstand the test condition without being cooled. When analysing transpiration cooling, however, with regard to its influencing parameters, e.g. coolant mass flow rate, the non-cooled side does not provide an ideal non-cooled reference, because the surface materials are different and their thermal and radiation properties as well, in general. Furthermore, the thickness of the surface layer is different as is the structure beneath. On the non-cooled side the model interior is filled with insulation, while there is open space below the porous sample. A more reliable non-cooled reference requires measurement on the porous sample itself.

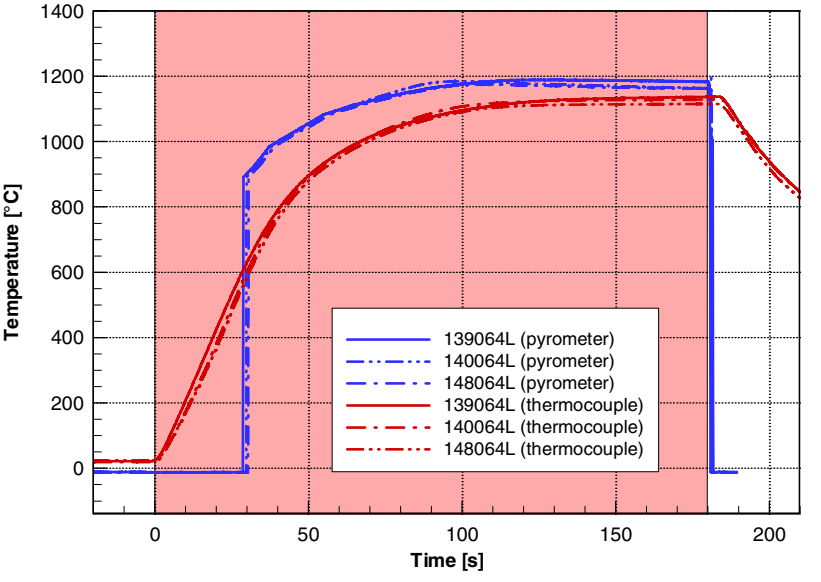

Fig. 19. Pyrometer and thermocouple measurements at the reference location from three tests at $\alpha = 30°$

Therefore, reference tests without coolant were included in the test matrix. Since the variation of coolant parameters was investigated on "Standard C/C", the same material was used for the non-cooled reference tests.

Figure 20 shows the results of temperature measurements on the top and rear side of the porous sample during the non-cooled reference test at a model inclination of 20°. The temperature on the top surface which is exposed to the flow has been taken from the infrared camera measurement, while the temperature on the bottom was measured by a thermocouple. At the end of the test the top surface is heated up to 980°C, which it by 35 K lower than the temperature on the non-cooled side of the model (see Fig. 18) due to the different materials' thermal properties. The temperature at the bottom reaches 732°C. The temperature difference between top and bottom side is significantly higher than measured for the cover plate which is mainly caused by the sample's thickness of 6 mm compared to a thickness of 3 mm for the cover plate.

Without coolant flow the sample's porosity is not beneficial, since it enables hot gas penetration into the reservoir. Therefore, the temperature inside the reservoir increases to 402°C at the end of the test, still increasing.

The surface temperature distribution is very homogeneous at the end of the reference test as comes out from the infrared image in Fig. 21. There are no temperature differences observed on the cover plate in lateral direction. Only the sample and its frame show slightly different temperatures, the sample due to its different emissivity value, the frame due to a different surface coating.

Figure 21b shows the same sample (Standard C/C) in a test with transpiration cooling. While the temperatures on the non-cooled side remain unchanged as expected, there are significant changes on the cooled side. The temperature of the sample itself is considerably reduced. In the wake of the sample, the cover plate is cooled as well. The sequence of infrared images in Fig. 22 shows that the differences between the cooled and non-cooled sides are even more obvious during the test. After 90 s of testing considerable differences are visible up the downstream end of the model. This region shrinks to about a quarter of its length at the end of the test.

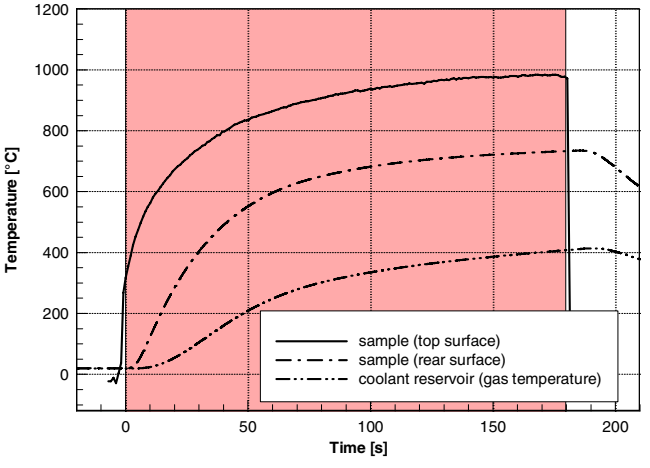

Fig. 20. Temperature measured on sample S1 and in the reservoir during the non-cooled reference test at $\alpha = 20°$

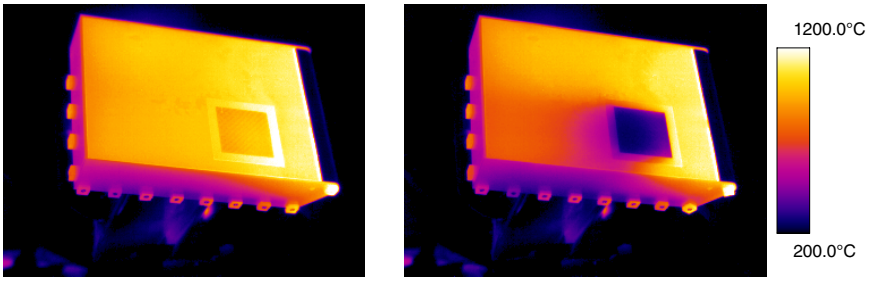

(a) non-cooled (b) cooled by 0.4 g/s N_2

Fig. 21. Infrared images at the end of a test with and without coolant flow (sample S1, $\alpha = 20°$, flow from right to left)

In the centre of the sample the temperature increases up to 280°C as shown in Fig. 23. Compared to the non-cooled reference test this is a reduction by about 700 K. Although the surface temperature did not reach a steady state condition after 180 s, the reduction is quite impressive. It becomes even more impressive when considering that a small part is caused by a gradual increase of the coolant's temperature.

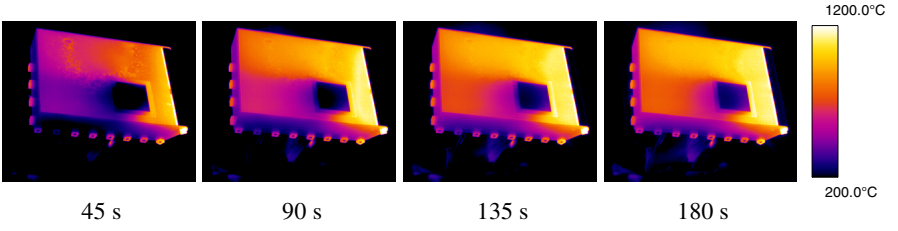

Fig. 22. Sequence of infrared images (sample S1, cooled by 0.4 g/s N_2, $\alpha = 20°$, flow from right to left)

During the test the coolant inside the reservoir heats up by about 65 K. The corresponding heat is mainly transferred along the side walls of the reservoir. It could hardly be avoided, since the reservoir had to be designed rigid with pressure-tight side walls and it had to be placed close to the hot surface.

When the model's inclination is increased to 30°, the observations are similar, but on a higher temperature level. Comparison of the infrared images in Fig. 24 from tests with and without coolant flow shows no differences in the temperature distribution on the reference side. For the non-cooled test the complete surface is homogeneously heated without obvious lateral temperature gradients. Again, cooling considerably affects the temperature evolution of the sample and the parts of the cover plate located downstream of the sample. As indicated by the sequence of infrared images in Fig. 25 the differences between the cooled and non-cooled parts are most significant after 45 and 90 seconds. Towards the end of the test the region with obvious differences becomes smaller. Due to the different coolant mass flow rates a direct comparison of the influence of transpiration cooling in the wake of the sample is not possible.

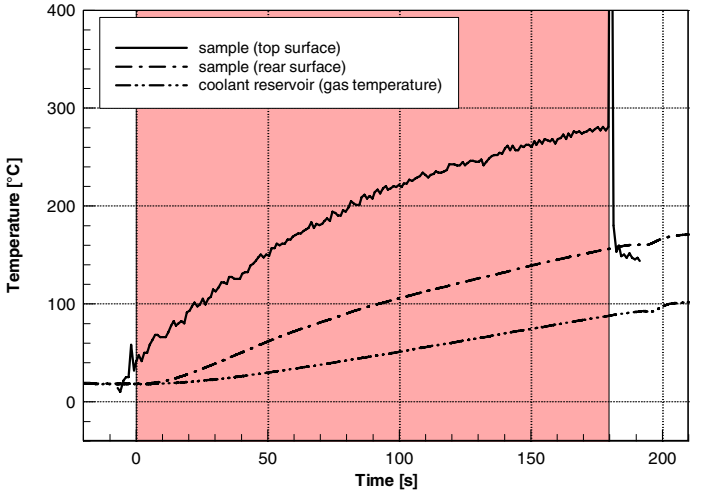

Fig. 23. Temperature measured on sample S1 and in the reservoir (cooled by 0.4 g/s N_2, $\alpha = 20°$)

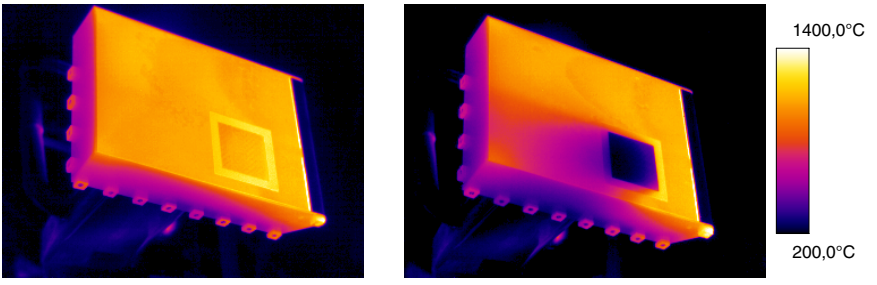

(a) *non-cooled* (b) *cooled by 0.8 g/s N_2*

Fig. 24. Infrared images at the end of a test with and without coolant flow (sample S2, $\alpha = 30°$, flow from right to left)

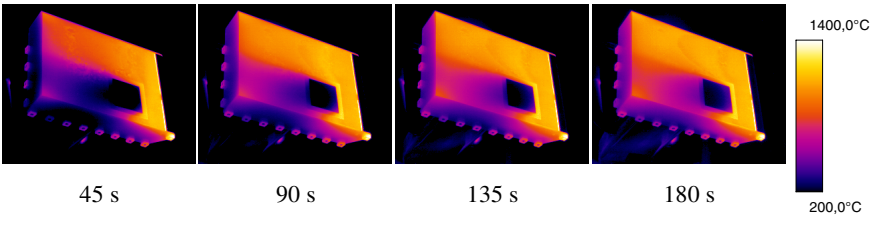

Fig. 25. Sequence of infrared images (Sample S2, cooled by 0.8 g/s N_2, $\alpha = 30°$, flow from right to left)

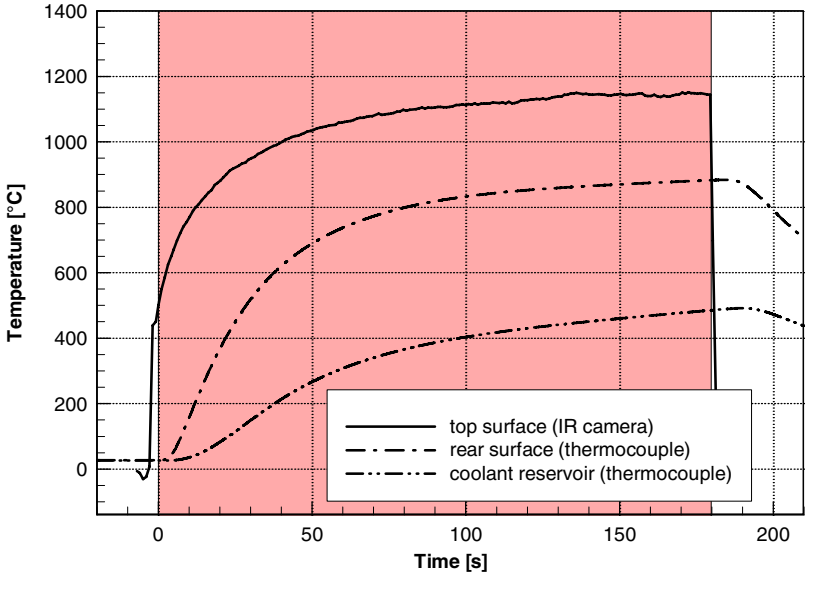

Fig. 26. Temperature measured on sample S2 and in the reservoir during the non-cooled reference test at $\alpha = 30°$

A temperature of 1145°C is reached in the centre of the sample at the end of the non-cooled reference test as shown in Fig. 26. Again, this value is slightly below the corresponding value on the reference side where a value of 1170°C was measured (see Fig. 19). The temperature on the rear side increases to 880°C. Again, there is considerable heating of the reservoir due to hot gas penetration which causes a temperature of close to 500°C at the end of the test.

When cooling the sample with 0.8 g/s nitrogen the surface temperature in the centre of the sample reaches 250°C after 180 seconds which is a reduction by 900 K compared to the non-cooled test (see Fig. 27). At the same time the bottom temperature is 130°C. The gas in the reservoir gradually increases by about the amount than at the lower angle of attack which confirms the assumption that the heat is mainly transferred through the side walls of the reservoir.

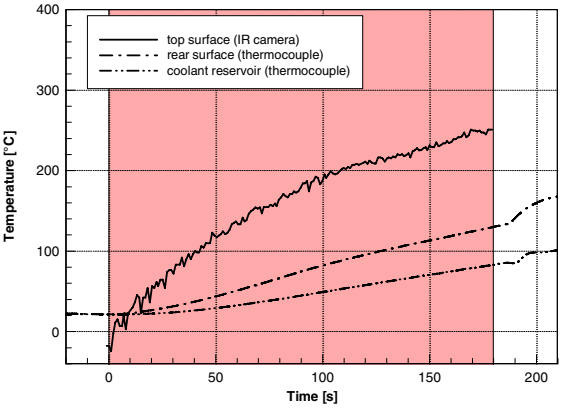

Fig. 27. Temperature measured on the sample and in the reservoir (Sample S2, cooled by 0.8 g/s N_2, $\alpha = 30°$)

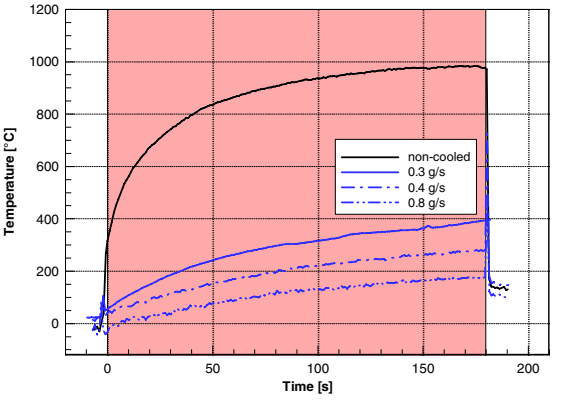

Fig. 28. Temperature measured in the centre of the sample for different coolant mass flow rates (sample S1 and S3, N_2, $\alpha = 20°$)

For the two heat loads different mass flow rates were applied using nitrogen as coolant on“standard-C/C” samples. For $\alpha = 20°$ mass flow rates of 0.3 g/s, 0.4 g/s and 0.8 g/s were tested. The corresponding temperatures that were measured by infrared camera in the centre of the samples are plotted in Fig. 28 and compared to the non-cooled reference test.

Even for the lowest mass flow rate of 0.3 g/s the temperature at the end of the test is remarkably reduced by about 590 K. The final temperature reached is 390°C which is below the material’s high temperature limit of operation. By increasing the mass flow rate to 0.4 g/s the final temperature is further reduced by 110°C to 280°C. In order to reduce the temperature by the same amount again, the mass flow rate has to be doubled to 0.8 g/s. The values show that the cooling potential nonlinearly decreases with increasing mass flow rate. While 0.4 g/s of nitrogen enable a temperature reduction of 700 K, another 0.4 g/s added on top have a potential for 110 K only.

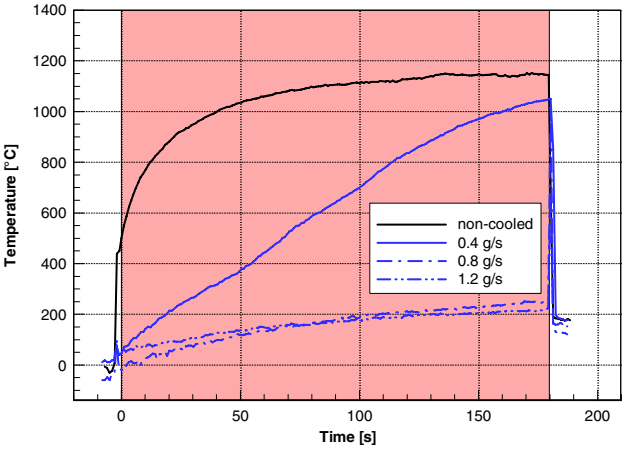

Fig. 29. Temperature measured in the centre of the sample for different coolant mass flow rates (sample S2, N_2, $\alpha = 30°$)

At an angle of attack of 30° the effect is even more pronounced. Figure 29 shows the temperatures that were measured for coolant mass flow rates of 0.4 g/s, 0.8 g/s, and 1.2 g/s. At a mass flow of 0.4 g/s the coolant is not able to reduce the surface temperature permanently. Although the surface temperature is below the temperature that was measured without cooling throughout the complete test, the final temperature is only 100 K below the non-cooled case. Furthermore, it is still increasing indicating that the steady state level will be very close to the non-cooled case. When the coolant’s mass flow rate is doubled to 0.8 g/s, cooling becomes effective by reducing the final temperature to 250°C. When adding another 0.4 g/s the temperature is reduced by 33 K only.

The results obtained for different mass flow rates indicate that up to a certain amount transpiration cooling is ineffective, like the 0.4 g/s case in Fig. 29. At high mass flow rates cooling is again ineffective, because a particular amount of coolant is wasted, since it hardly contributes to a reduction of surface temperature. There must

be an optimal regime in between with a considerable reduction of surface temperature at moderate mass flow rates. Of course, this optimum depends on the heat load and the porous material.

For $\alpha = 20°$ and "standard-C/C" samples it was tried to assess the optimal mass flow rates for the three available coolants, nitrogen, argon, and helium. During the corresponding tests the mass flow rate was increased gradually and the temperature response of the sample was observed. The optimal mass flow rate was found when the trend of the sample's temperature turned from increasing to decreasing. By that, the optimal mass flow rates were identified to 0.4 g/s for nitrogen, 0.2 g/s for helium, and 0.5 g/s for argon.

Afterwards, regular tests at constant coolant flow were performed for the optimal mass flow rates with an increased testing time of 240 seconds. The corresponding temperature measurements are compared in Fig. 30.

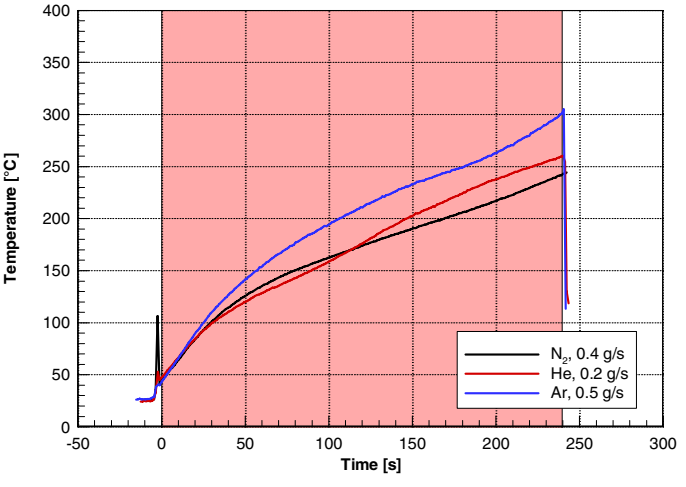

Fig. 30. Temperature measured in the centre of the sample for different coolants at optimal mass flow rates (sample S3, $\alpha = 20°$)

Since the optimal mass flow rates were found by an identical procedure, the temperature histories are similar, but there are still some differences. Although argon was supplied at higher mass flow rate compared to nitrogen and helium, it still provides the highest temperatures on the sample. Nitrogen is performing slightly better than helium at optimal mass flow rate, but helium has the advantage of the lowest mass flow rate.

3.5 Summary and Conclusions

Several test campaigns were performed in the arc heated facilities L2K and L3K in order to qualify the concepts for transpiration cooling that were described in section 6. In two preparatory campaigns useful results were obtained that helped to optimize the experimental setup and the operation of auxiliary systems as well.

For the final test campaign in the L3K facility a flat plate model was used which allowed for integration of square porous samples on one side. The remaining part of the surface was made of C/C-SiC, a well qualified reusable thermal protection material which provided the opportunity to compare the results of transpiration cooling with a qualified conventional thermal protection technology. The model was instrumented for temperature measurements. In addition to thermocouple measurements in the interior the surface was observed by infrared cameras and pyrometers. The porous sample was integrated into a coolant reservoir, which could continuously be supplied by coolant gas from outside the test chamber. A mass flow controller was integrated into the supply line that allowed for constant feeding at specified mass flow rate.

During the test campaign three different porous materials and three different coolants were applied. In addition, the coolant's mass flow rate was varied systematically for one sample material. Tests at two angles of attack, i.e. 20° and 30°, allowed to generate different heat loads. Individual tests were performed at constant coolant mass flow rate. The temperature measurements on the cooled samples were compared to the results of reference tests without cooling.

From the tests at different coolant mass flow rates it was found that for very low rates transpiration cooling is not effective. At a given heat load the increase of surface temperature is delayed only, but at the final temperatures are very close to the non-cooled case. At high mass flow rates cooling is ineffective as well, because a particular amount of coolant does not contribute to a reduction of surface temperature. In between there is optimum mass flow rate which for a "standard-C/C" sample at a model inclination of 20° was identified to 0.4 g/s for nitrogen cooling, 0.2 g/s for helium cooling and 0.5 g/s for argon cooling. Considering the sample's surface area these values correspond to blowing ratios of 0.027 for nitrogen, 0.014 for helium, and 0.034 for argon. These blowing ratios are much smaller smaller than those obtained for film cooling which again demonstrates the huge potential of transpiration cooling.

If only the coolant's mass is taken into account, helium performs best among the three coolants. In case of real applications other parameter might become decisive again, due to limitations to storage volume or reservoir pressures. If e.g. reservoir pressure is limiting variable, the optimum mass flow rates must be weighed by the coolant's molecular mass, yielding 3.96 mole/(m^2s) for nitrogen, 13.9 mole/(m^2s) for helium, 3.47 mole/(m^2s) for argon, and reversing the performance order.

References

1. Esser, B., Gülhan, A., Schäfer, R.: Experimental Investigation of Thermal Fluid/Structure Interaction in High Enthalpy Flow. In: 5th Europ. Symp. on Aerothermodynamics for Space Vehicles, Cologne, ESA SP-563, pp. 275–280 (2004)
2. Gnemmi, P., Schäfer, H.J.: Grundlegende Untersuchungen zur Seitenstrahlsteuerung: Numerische Simulation der Wechselwirkung eines Kaltgasstrahls mit der Außenströmung. ISL, Saint Louis (2004)
3. Gülhan, A., Esser, B.: A Study on Heat Flux Measurements in High Enthalpy Flows. In: 35th AIAA Thermophysics Conference, June 11-14, Anaheim, CA, AIAA (2001)

4. Gülhan, A., Esser, B.: Arc-Heated Facilities as a Tool to Study Aerothermodynamic Problems of Reentry Vehicles. In: Lu, F.K., Marren, D.E. (eds.) Advanced Hypersonic Test Facilities. Progress in Astronautics and Aeronautics, AIAA, vol. 198, pp. 375–403 (2002)
5. Hald, H.: Faserkeramiken für heiße Strukturen von Wiedereintrittsfahrzeugen – Simulation, Test und Vergleich mit experimentellen Flugdaten. Ph.D. thesis, Univ. Stuttgart (2001)
6. Holden, M.S.: A study of flow separation in regions of shock wave – boundary layer interactions in hypersonic flow. AIAA Paper 78-1169 (1978)
7. Jung, K.: Mehrreihige Filmkühlung an gekrümmten Oberflächen. Dissertation, Univ. Darmstadt (2001)
8. Kohli, A., Thole, K.A.: Entrance Effects on Diffused Film-Cooling Holes. ASME, New York (1998)
9. Kovar, A., Schülein, E.: Comparison of experimental and numerical investigations on side jets in a supersonic cross flow. Royal Aeronautical Society, London (2004)
10. Krenkel, W.: Applications of Fibre Reinforced C/C-SiC Ceramics. Ceramic Forum International 80(8), E31–E38 (2003)
11. Lezuo, M.K.: Wärmetransport in H2-transpirativ gekühlten Brennkammerkomponenten, Ph.D. thesis, RWTH Aachen (1998)
12. Meinert, J.: Haftreibung und Wärmeübergang in einer turbulenten Grenzschicht bei Fremdgastranspiration. VDI, Düsseldorf (2000)
13. Radespiel, R., Longo, J.M.A., Brück, S.: Efficient numerical simulation of complex 3D flows with large contrast. In: 77th AGARD Fluid Dynamics Panel, Meeting and Symposium on Progress and Changes in CFD Methods and Algorithms, Sevilla, AGARD-CP-578, pp. 1–33 (1995)
14. Serbest, E.: Untersuchungen zur Anwendung der Effusionskühlung bei Raketenbrennkammern., Ph. D. Thesis, RWTH Aachen (2002)
15. Wittig, S., Thole, K.A.: Transonic Film-cooling Investigations: Effects of Hole Shapes and Orientations, ASME, New York, 35/96-222 (1996)